

IMPLANTATION OF ENERGETIC D⁺ IONS INTO CARBON DIOXIDE ICES AND IMPLICATIONS FOR OUR SOLAR SYSTEM: FORMATION OF D₂O AND D₂CO₃

CHRIS J. BENNETT^{1,2,3}, COURTNEY P. ENNIS^{1,4}, AND RALF I. KAISER^{1,2}

¹ Department of Chemistry, University of Hawai'i at Mānoa, Honolulu, HI 96822, USA; ralfk@hawaii.edu

² Institute for Astronomy and NASA Astrobiology Institute, 2680 Woodlawn Drive, University of Hawai'i, Honolulu, HI 96822, USA

Received 2014 July 7; accepted 2014 August 8; published 2014 September 24

ABSTRACT

Carbon dioxide (CO₂) ices were irradiated with energetic D⁺ ions to simulate the exposure of oxygen-bearing solar system ices to energetic protons from the solar wind and magnetospheric sources. The formation of species was observed online and in situ by exploiting FTIR spectroscopy. Molecular products include ozone (O₃), carbon oxides (CO₃(C_{2v}, D_{3h}), CO₄, CO₅, CO₆), D₂-water (D₂O), and D₂-carbonic acid (D₂CO₃). Species released into the gas phase were sampled via a quadrupole mass spectrometer, and possible minor contributions from D₂-formaldehyde (D₂CO), D₄-methanol (CD₃OD), and D₂-formic acid (DCOOD) were additionally identified. The feasibility of several reaction networks was investigated by determining their ability to fit the observed temporal column densities of 10 key species that were quantified during the irradiation period. Directly relevant to the CO₂-bearing ices of comets, icy satellites in the outer solar system, and the ice caps on Mars, this work illustrates for the first time that D₂-water is formed as a product of the exposure of CO₂ ices to D⁺ ions. These findings provide strong support for water formation from oxygen-bearing materials via non-thermal hydrogen atoms, and predict reaction pathways that are likely to be unfolding on the surfaces of asteroids and the Moon.

Key words: astrochemistry – infrared: general – methods: laboratory: solid state – molecular processes – planets and satellites: general – radiation mechanisms: non-thermal

Online-only material: color figures

1. INTRODUCTION

Carbon dioxide (CO₂) has been detected throughout our solar system. It is commonly released from comets at abundances up to 30% relative to water, as was recently determined using the *Akari* satellite, which allowed for the simultaneous measurement of water (H₂O), carbon monoxide (CO), and carbon dioxide (CO₂; Ootsubo et al. 2012). CO₂ is also observed on icy moons within the solar system. In the Jovian system, CO₂ has been identified on the surfaces of Europa (Smythe et al. 1998), Ganymede (McCord et al. 1998), and Callisto (Hibbitts et al. 2000); Callisto also exhibits a tenuous atmosphere possessing a component of CO₂ (Carlson 1999). In the Saturnian system, CO₂ has been probed on the surface of Enceladus, Dione, Hyperion, Iapetus, and Phoebe (Buratti et al. 2005; Clark et al. 2005, 2013; Brown et al. 2006; Cruikshank et al. 2010). It has also been identified as a component of Rhea's tenuous atmosphere (Teolis et al. 2010). In both the Jovian and Saturnian systems, the surface temperature of these moons is typically above the point that CO₂ would be stable in the solid state (> 100 K). This may point to an in-situ production; several authors have noted that the abundance of CO₂ may be correlated (or anti-correlated) to radiation induced from the magnetosphere, as well as the abundance of water and dark carbonaceous material (McCord et al. 1997; Hibbitts et al. 2000, 2003; Cruikshank et al. 2010; Pinilla-Alonso et al. 2011; Clark et al. 2013; Scipioni et al. 2013). Note that the persistence of CO₂ on icy bodies at such temperatures could be explained by carbon dioxide being trapped beneath less volatile water ices, existing in a less volatile clathrate form, or being physisorbed on refractory solids (Chaban

et al. 2007; Hibbitts & Szanyi 2007; Cruikshank et al. 2010). Within the Uranian system, CO₂ is only identified on Ariel, Umbriel, and Titania—the satellites exposed to magnetospheric particles (CO₂ has not been identified on Oberon which spends the majority of its orbit beyond the magnetosphere)—whereas water is sampled throughout (Grundy et al. 2003, 2006). Triton, which accounts for >99% of the mass of the natural Neptunian satellites, also exhibits absorption features attributed to CO₂ and H₂O (Cruikshank et al. 1993; Quirico et al. 1999).

Within the terrestrial planets, CO₂ is also commonplace, being the most abundant species within the atmospheres of both Mars and Venus. While the latter is too warm for ice to form, the polar ice caps of Mars feature extensive perennial H₂O features that are seasonally covered with up to a few meters of CO₂ ice, which potentially consists of up to 0.1% H₂O by weight (Hansen 1999, 2013; Hansen et al. 2010; Bibring et al. 2004). The reduced atmosphere and magnetic field on Mars leaves the caps exposed to solar and galactic cosmic radiation. Radiolytic processing could produce the new molecules that are detected by spacecraft such as *MAVEN*, which is currently investigating the Martian atmosphere (Strazzulla et al. 2005; Wu et al. 2011). Alternatively, such processes could act as loss mechanisms for these species to escape the Martian atmosphere (Lundin et al. 2007; Lammer et al. 2013). Several telescopes currently operational are capable of detecting CO₂ within the atmosphere of exoplanets, as demonstrated by its recent discovery within the emission spectrum of HD 189733b, alongside the detection of H₂O, methane (CH₄), and CO (Selsis et al. 2008; Swain et al. 2010).

Because the majority of these environments are exposed to energetic particles from the solar wind or galactic cosmic rays, and magnetospheric ions and electrons in the case of many planetary satellites (Johnson 1990; Kaiser & Roessler 1997; Kaiser et al. 1997; Madey et al. 2002; Bennett et al. 2013b), many of the products formed from the irradiation of CO₂ and mixed

³ Present address: Chemistry and Biochemistry, Georgia Institute of Technology, 901 Atlantic Drive, Atlanta, GA 30332-0400, USA.

⁴ Present address: Australian Synchrotron, 800 Blackburn Road, Clayton, VIC 3168, Australia.

CO₂:H₂O ices are expected to be present and detectable within these environments—such as formaldehyde, H₂CO, the cyclic isomer of carbon trioxide, CO₃(C_{2v}), and carbonic acid, H₂CO₃ (e.g., Hage et al. 1998; Strazzulla et al. 2005; Wu et al. 2011). Several groups have verified the production of H₂CO₃ via the irradiation of mixed ices by energetic ions (Moore & Khanna 1991; Brucato et al. 1997; Strazzulla et al. 2005; Peeters et al. 2010; Pilling et al. 2010), electronic electrons (Zheng & Kaiser 2007; Jones et al. 2014a), and UV photons (Wu et al. 2003). The production of CO, O₃, and CO₃(C_{2v}) was typically observed in these studies. Oba et al. (2010) were additionally able to identify the production of carbonic acid when CO ices were exposed to OH radicals.

Next, we consider previous experiments where pure CO₂ ices were exposed to H⁺, D⁺, or D₂⁺ ions. Studies by Garozzo et al. (2008) and Raut & Baragiola (2013) utilizing relatively high energy H⁺ ions (50–100 keV) confirmed the production of CO, O₃, and CO₃(C_{2v}), however, only the former additionally reported the formation of H₂CO₃. Similarly, several studies focused on the energy range relevant to the majority of solar wind H⁺ ions (1–5 keV range). Brucato et al. (1997) exposed CO₂ ices to 1.5 keV H⁺ ions, and were able to identify CO, O₃, CO₃(C_{2v}), and H₂CO₃. Ennis et al. (2011b) utilized 5 keV D₂⁺ ions (which split upon impact with the ice to neutral (D) and ion (D⁺) each bearing about 2.5 keV) and were able to identify D₂-carbonic acid and D₂-water during the subsequent warm-up of the ice. In a more recent study, Sivaraman et al. (2013) exposed CO₂ ices to 1.5 keV H⁺ and 2.1 keV D⁺ ions, but did not report any products that incorporated these ions. Instead they reported the formation of CO, O₃, CO₃(C_{2v}), and CO₃(D_{3h}). These studies indicate the potential for the production of H₂CO₃ within not only mixed ices containing CO₂, but also pure ices exposed to radiation. Since H₂CO₃, for example, is much less volatile than CO₂, it can remain on bodies such as icy satellites or the polar caps of Mars for increased periods of time (Peeters et al. 2010). Due to the coexistence of CO₂ and H₂O in a number of these environments, it is essential to investigate the full reaction network that dictates the abundance and production of both species. Emerging work has demonstrated that irradiation of CO₂ via low energy 5 keV D₂⁺ ions leads to the formation of D₂-water (Ennis et al. 2011b), this work is continued here, where CO₂ ice is exposed to pure 5 keV D⁺ ions to probe the formation of D₂-carbonic acid and D₂-water.

2. EXPERIMENTAL

The experimental procedure and set-up for the present study has been described previously (Bennett et al. 2005; Ennis et al. 2011a). An ultra-high vacuum chamber was utilized for the experiments, evacuated to $9.7 \pm 0.5 \times 10^{-11}$ torr. A closed-cycle helium refrigerator was used to cool a highly polished silver target down to 12.0 ± 0.7 K to act as the substrate for ice deposition. Pure CO₂ gas (BOC gases; 99.999%) was deposited through a glass capillary array positioned 5 mm from the target for 6 minutes, while the background chamber pressure was held at $1.0 \pm 0.1 \times 10^{-8}$ torr. Once prepared, the ices were monitored online and in situ by an FTIR spectrometer (Nicolet 6700; liquid nitrogen cooled MCTB detector) operating in absorption–reflection–absorption mode at an incident angle of 75°. Each infrared spectrum over the range of 4000–400 cm⁻¹ was collected for 2 minutes (196 scans) at a resolution of 4 cm⁻¹ (except the background which was collected for 784 scans; taken to determine the intensity of the incident radiation under our configuration). The thickness of the CO₂ ice was then

inferred from a modification of the Beer–Lambert Law (Bennett et al. 2004), from which the change in path-length due to the refractive index of the ice ($n = 1.21$ at 10 K measured by Satorre et al. 2008) was taken into account. The area of the $\nu_1 + \nu_3$ combination band centered at 3708 cm⁻¹ was integrated, along with the experimentally determined intensity (*A*-value) of 1.4×10^{-18} cm molecule⁻¹ for the band (Gerakines et al. 1995), to derive a column density of $1.6 \pm 0.1 \times 10^{18}$ molecules cm⁻². Combined with the experimentally measured density at 10 K of 0.98 g cm⁻³ (Satorre et al. 2008) this yielded an ice thickness of 1.2 ± 0.1 μm.

Once prepared, the CO₂ frosts were then exposed to irradiation from 5 keV D⁺ ions for 110 hr generated in an ion source (SPECS IQE 12/38), which was separated by a series of differentially pumped stages so that during operation of the ion beam the pressure in the analysis chamber did not exceed $1.0 \pm 0.1 \times 10^{-10}$ torr. The ions themselves were generated via electron impact on pure molecular deuterium gas (99.8% D₂; ion isotopes) at a pressure of $5.0 \pm 0.2 \times 10^{-4}$ torr over the entire irradiation period, which was necessarily high to obtain a sufficient beam current. Since D₂⁺ and D₃⁺ ions are also initially present in the beam, a Wien filter (0.12 T; Specs WF-IQE) was incorporated to ensure that our beam consisted solely of 5 keV D⁺ ions. The beam current was measured at 13.9 ± 2.0 nA on the target, covering an area of 0.5 ± 0.1 cm². This translates to $8.70 \pm 1.25 \times 10^{10}$ D⁺ ions s⁻¹ and a total exposure of the CO₂ ice to $3.4 \pm 0.5 \times 10^{16}$ D⁺ ions over the irradiation period. The TRIM code (Ziegler et al. 2010) was used to simulate the energy transfer, processes, and penetration depths of 5 keV D ions (2.014 amu) impinging on a solid CO₂ target of density 0.98 g cm⁻³, using the SRIM-2008 stopping powers. Here, the average penetration depth was determined to be 236 ± 82 nm, with >99.9% of the ions coming to rest within 500 nm of the ice; this is notably much lower than the estimated ice thickness. The irradiated ice sample was then held for a further 15 minutes at 12.0 ± 0.7 K, prior to being warmed to 300 K, at a rate of 0.5 K minute⁻¹. The gas phase was sampled online and in situ throughout the experiment via a quadrupole mass spectrometer (QMS; Balzer QMG 420) operating in the residual gas analyzer mode, and ionizing neutral species via electron impact (100 eV).

3. RESULTS

The infrared spectrum (4000–500 cm⁻¹) of pristine carbon dioxide ice is shown in Figure 1(a), along with the spectrum obtained after the irradiation period, both held at 11 K. Figure 1(b) shows a subtraction spectrum of the same spectra to show more clearly some of the observed species. Band positions and assignments of the pure carbon dioxide ice are listed in Table 1, whereas those for the new species identified upon irradiation are listed in Table 2. Spectra are also shown during the heating period in Figure 2 chosen at the same temperatures as in Ennis et al. (2011b) for comparison. In addition, Figure 3 shows the temporal evolution of the relative band areas for selected species during the heating of the ice.

3.1. Infrared Spectrum of Pristine CO₂ Ice

The only absorption bands identified in the pristine spectra are attributed to the ground-state linear carbon dioxide molecule (CO₂; X¹Σ_g⁺) and its most abundant naturally occurring isotopomers: ¹³CO₂ and ¹⁸OCO (Table 1; Figure 1(a), black line). The most intense feature is the asymmetric stretching band (ν_3) found at 2339 cm⁻¹ for CO₂ (with associated lattice bands at

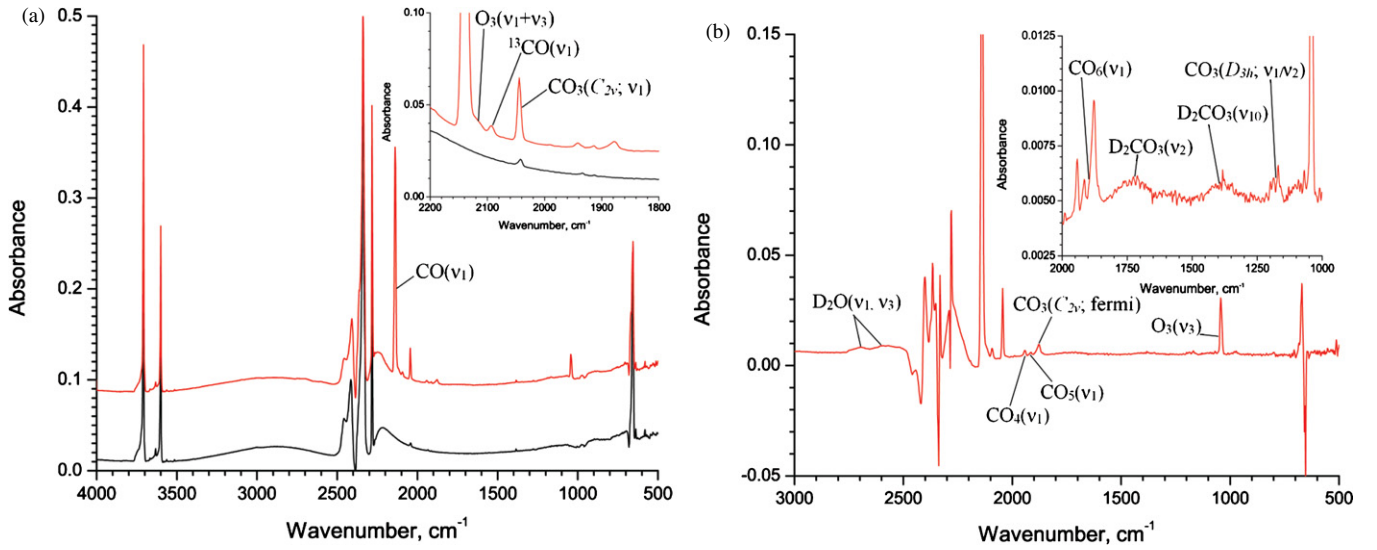


Figure 1. Infrared spectra of CO₂ ices: (a) over the range 4000–500 cm⁻¹ before (black line) and after irradiation (red line), the inset illustrates some of the newly formed molecules over the range 2200–1800 cm⁻¹, (b) difference spectrum before and after irradiation illustrating more clearly the peak positions of newly formed molecules over the range 3000–500 cm⁻¹, the inset showing more clearly some of the spectral features in the range of 2000–1000 cm⁻¹. (A color version of this figure is available in the online journal.)

Table 1
Infrared Absorptions of the CO₂ Ice Before Irradiation

Frequency (cm ⁻¹)	Assignment	Characterization
3709 (3715, 3738)	CO ₂ (ν ₁ + ν ₃)	Combination band
3667	¹⁸ OCO (ν ₁ + ν ₃)	Isotope combination band
3633	¹³ CO ₂ (ν ₁ + ν ₃)	Isotope combination band
3601 (3608, 3633)	CO ₂ (2ν ₂ + ν ₃)	Combination band
3564	¹⁸ OCO (2ν ₂ + ν ₃)	Isotope combination band
3515	¹³ CO ₂ (2ν ₂ + ν ₃)	Isotope combination band
2339 (2415, 2458)	CO ₂ (ν ₃)	Asymmetric stretch
2328	¹⁸ OCO (ν ₃)	Isotope asymmetric stretch
2283	¹³ CO ₂ (ν ₃)	Isotope asymmetric stretch
2042	CO ₂ (ν ₂ ³ 03 ¹ 0) ^a	Fermi resonance
1990, 2006	CO ₂ (ν ₂ ³ 03 ³ 0) ^a	Fermi resonance
1913, 1933	CO ₂ (ν ₁ ν ₂ 11 ¹ 0) ^a	Fermi resonance
1385	CO ₂ (ν ₂ ² 02 ⁰ 0) ^a	Fermi resonance
1278	CO ₂ (ν ₁ 10 ⁰ 0) ^a	Fermi resonance
659, 653	CO ₂ (ν ₂)	In-plane/out-of-plane bend
638	¹³ CO ₂ (ν ₂)	Isotope in-plane/out-of-plane bend

Notes. Values in parenthesis indicate approximate positions of lattice bands, which are visible only for the most intense peaks.

^a As denoted by Rodriguez-Garcia et al. (2007). These bands are very weak; their absorptions were removed via deconvolution of the peaks in order to determine the column densities of the products formed (see Table 2).

2415 and 2458 cm⁻¹), 2328 cm⁻¹ for ¹⁸OCO, and 2283 cm⁻¹ for ¹³CO₂. A double peak for the in- and out-of-plane bend (ν₂) is located at 659/651 cm⁻¹ for CO₂, with the corresponding ¹³CO₂ band identified at 638 cm⁻¹. The (ν₁ + ν₃) combination band is found at 3709 cm⁻¹ (along with libration bands at 3715 and 3738 cm⁻¹) for CO₂, with bands from the ¹⁸OCO and ¹³CO₂ isotopomers also visible at 3667 and 3633 cm⁻¹, respectively. The (2ν₂ + ν₃) combination band lies at 3601 cm⁻¹ (with libration bands centered at 3608 and 3633 cm⁻¹), whereas the associated isotopomer absorptions are found at 3564 and 3515 cm⁻¹ for ¹⁸OCO and ¹³CO₂, respectively. In addition, a number of bands arising from Fermi interactions are identified. While those identified at 1278 and 1385 cm⁻¹ are commonly

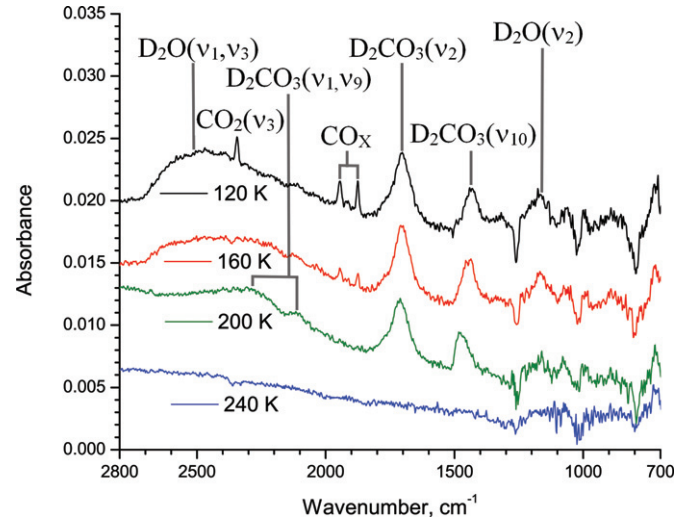


Figure 2. FTIR spectra over the range of 2800–700 cm⁻¹ of the residual species after the CO₂ ice has sublimated at temperatures of 120 K (black line), 160 K (red line), 200 K (green line), and 240 K (blue line). Approximate positions of bands due to D₂O, D₂CO₃, trapped CO₂, and CO_x (x = 3–6) species are indicated.

(A color version of this figure is available in the online journal.)

reported, several weaker bands located at 2042, 2006/1990, 1933/1913 were also identified. Here, we assign these features to Fermi resonances based on their calculated values and listed in Table 1 with notation corresponding to Rodriguez-Garcia et al. (2007).

For each of the values reported in Table 1, good agreement is found with values reported previously in the literature (Cahill 1977; Sandford & Allamandola 1990; Gerakines et al. 1995; Bennett et al. 2004, 2010; Garozzo et al. 2008; Seperuelo Duarte et al. 2009; Ennis et al. 2011b; Raut & Baragiola 2013; Sivaraman et al. 2013; Jones et al. 2014a). The only notable exception is that in the present study little evidence is found to support the slipped CO₂ dimer as reported by Sivaraman et al. (2013), which was identified at 2328 cm⁻¹ for CO₂ ices prepared

Table 2
Band Positions and Assignments of New Species

	Brucato et al. (1997)	Garozzo et al. (2008)	Ennis et al. (2011b)	Raut & Baragiola (2013)	Sivaraman et al. (2013)	Present Study
Experimental conditions						
Ice temperature	10–20 K	16 K	11 K	25 K, 50 K	30 K, 80 K	12 K
Radiation source	1.5 keV H ⁺	50–100 keV H ⁺	5 keV D ₂ ⁺	100 keV H ⁺	1.5 keV H ⁺ , 2.12 keV D ⁺	5 keV D ⁺
Dose ^a	52	30–624	13600	...	124–957	1080
Positions/assignments						
CO (ν_1)	2142	2139	2142	2140	2140	2139
¹³ CO (ν_1)	...	2093	2092	2094
O ₃ ($\nu_1 + \nu_3$)	2118
O ₃ (ν_3)	1040	1039	1040	1043	1042	1042
O ₃ (ν_2)	706 ^b
CO ₃ (C_{2v} ; ν_1)	2044	2045	2045	2044	2045	2044
CO ₃ (C_{2v} ; ν_{fermi})	1876	...	1879	1878
CO ₃ (C_{2v} ; ν_2)	1071	...
CO ₃ (C_{2v} ; ν_5)	971	975 ^b
CO ₃ (D_{3h} ; ν_1/ν_2)	1167	1169, 1189sh ^c
CO ₄ (ν_1)	1943
CO ₅ (ν_1)	1916
CO ₆ (ν_1)	1893
H ₂ CO ₃ /D ₂ CO ₃ (ν_1, ν_9)	2900–2600
H ₂ CO ₃ /D ₂ CO ₃ (ν_2)	1736	1719	1729br
H ₂ CO ₃ /D ₂ CO ₃ (ν_{10})	1490	1508	1385br
H ₂ CO ₃ /D ₂ CO ₃ (ν_3)	1302	1307
D ₂ O (ν_1, ν_3)	2701 ^d , 2741 ^d
Residue	$T = 250$ K	$T = 185$ K	$T = 120$ K [200 K]	$T = 120$ K [200 K]
H ₂ CO ₃ /D ₂ CO ₃ (ν_1, ν_9)	3040, 2860	...	[2262–2110]	[2500–2050]
H ₂ CO ₃ /D ₂ CO ₃ (ν_2)	1727	1719	1709 [1720]	1703 [1709]
H ₂ CO ₃ /D ₂ CO ₃ (ν_{10})	1503	1508	1433 [1486]	1433 [1475]
H ₂ CO ₃ /D ₂ CO ₃ (ν_3)	1304	1307	1330	1320 ^b
H ₂ CO ₃ /D ₂ CO ₃ (ν_{11})	1025
H ₂ CO ₃ /D ₂ CO ₃ (ν_7)	819
D ₂ O (ν_1, ν_3)	2730–2300	2710–2100
D ₂ O (ν_2)	1177

Notes. New species observed when pure CO₂ ices were exposed to 5 keV D⁺ ions in the present experiment, as well as comparisons to those in the literature where energetic H⁺/D⁺/D₂⁺ ions were used to generate products where these ions were incorporated into the products.

^a In units of eV molecule⁻¹.

^b Tentative assignment due to noise from spectrometer.

^c D₂O (ν_2) may also contribute to this peak.

^d D₂CO₃ (ν_1, ν_9) may also contribute to this peak.

at low temperature. We instead ascribe this feature to the (ν_3) band of ¹⁸OCO, on the basis that all additional bands attributed to this isotopomer combine to support its presence in the ice.

3.2. Infrared Spectrum of Irradiated CO₂ Ice

Exposure of CO₂ ice to 5 keV D⁺ ions leads to both electronic (S_e) and nuclear (S_n) interactions within the solid, with the former accounting for about 90% of the kinetic energy loss of the impinging particles. The infrared spectrum after the irradiation period is shown in Figure 1(a), red line, with the differences more visible in the subtraction spectra (Figure 2). The corresponding band positions and assignments are provided in Table 2, which additionally shows a comparison of the present study to other literature values reported for CO₂ ices exposed to keV energy H⁺, D⁺, or D₂⁺ ion sources.

Many of the species detected have been identified previously, for example, when mixed CO₂:H₂O ices were exposed to energetic electrons (Zheng & Kaiser 2007; Jones et al. 2014a), UV photons (Wu et al. 2003), or energetic ions (Moore & Khanna 1991; DelloRusso et al. 1993; Brucato et al. 1997; Strazzulla et al. 2005; Seperuelo Duarte et al. 2009; Peeters et al. 2010; Pilling et al. 2010), as well as pure CO₂ ices exposed to energetic electrons (e.g., Bennett et al. 2004), UV photons (Gerakines et al. 1996), and energetic ions (Brucato et al. 1997; Garozzo et al. 2008; Ennis et al. 2011a, 2011b; Raut & Baragiola 2013; Sivaraman et al. 2013; Table 2). Carbon monoxide (CO) is identified through its intense fundamental (ν_1) stretching mode at 2139 cm⁻¹, for which the ¹³CO isotopomer is also of sufficient abundance to be detected at 2094 cm⁻¹. The ozone molecule (O₃) is verified by absorptions arising at 1042 cm⁻¹ (ν_3). In addition, we find evidence for the (ν_2) fundamental at 706 cm⁻¹

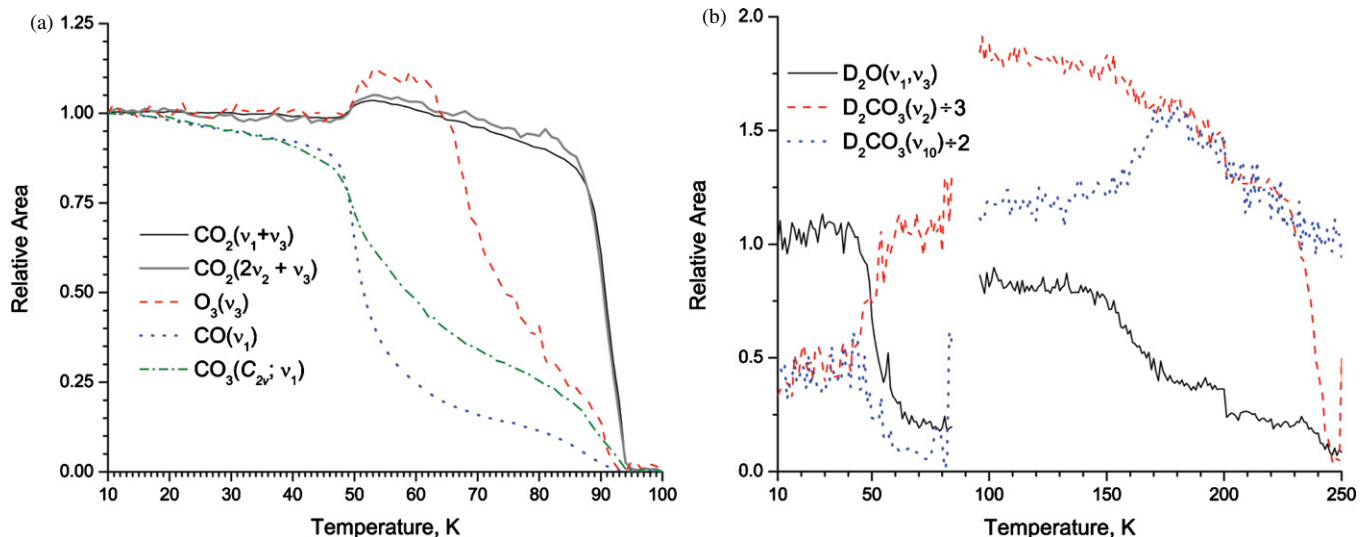


Figure 3. Temporal evolution of the band areas during the warm up period: (a) over the range of 10–100 K for CO₂ (black and blue lines), O₃ (red dashed line), CO (blue dotted line), and CO₃(C_{2v}) (green dash-dot line), (b) over the range of 10–250 K for D₂O (black line), D₂CO₃ (red dashed and blue dotted lines). Note that for D₂O and D₂CO₃, the areas were corrected by a factor to account for the different infrared intensities of the pure vs. isolated species (see Table 3 for details).

(A color version of this figure is available in the online journal.)

and (ν₁ + ν₃) combination band at 2118 cm⁻¹; the assignments are in good stead with values reported in the literature (e.g., Bennett & Kaiser 2005). The C_{2v} isomer of CO₃ is probed by its (ν₁) stretch at 2044 cm⁻¹, along with the (ν₅) band tentatively assigned to a feature at 975 cm⁻¹ and a Fermi resonance peak located at 1878 cm⁻¹. The D_{3h} isomer of CO₃ is revealed by its (ν₁/ν₂) stretch at 1169 cm⁻¹ (including a shoulder feature at 1189 cm⁻¹, which appears unassociated with the ν₂ band of D₂O). Previously this band had only been reported in CO₂ ices exposed to energetic ions by Sivaraman et al. (2013), where it was found at 1167 cm⁻¹ and in electron-irradiated CO₂ ices (Jamieson et al. 2006) at 1165 cm⁻¹.

In addition, we report for the first time the identification of higher carbon oxide species CO_x (x = 4, 5, 6) that were previously only reported in electron irradiated CO₂ ices. Here, the C_{2v} isomer of CO₄(ν₁) is identified at 1943 cm⁻¹, which is in good agreement with the previous assignment at 1941 cm⁻¹ (Jamieson et al. 2007a). Similarly, the C₂ isomer of CO₅(ν₁) is found at 1916 cm⁻¹, which is close to the previous location at 1912 cm⁻¹ (Jamieson et al. 2007b). Lastly, the C_s isomer of CO₆(ν₁) is found at 1893 cm⁻¹, whereas it was previously identified at 1876 cm⁻¹ (Jamieson et al. 2008); the small discrepancy in peak positions reported for CO₆ is likely a result of the deconvolution procedure used in each case.

Next, we focus on the detection of species that incorporate deuterium once the impinging ions and atoms have sufficiently slowed. Here, we find evidence for the most stable *cis*-form of deuterated carbonic acid, D₂CO₃, where the absorptions are found to be in good agreement with both theoretical and matrix isolated studies (Wight & Boldyrev 1995; Bernard et al. 2013; Reddy & Balasubramanian 2014). This species was previously identified as a product of mixed CO₂:D₂O ices exposed to electrons (Zheng & Kaiser 2007; Jones et al. 2014a), photons (Wu et al. 2003), and ion irradiation (Moore & Khanna 1991; DelloRusso et al. 1993; Brucato et al. 1997; Strazzulla et al. 2005; Seperuelo Duarte et al. 2009; Peeters et al. 2010; Pilling et al. 2010). It was also identified, along with its deuterated counterpart, in CO ices exposed to OD radicals in experiments carried out by Oba et al. (2010). As noted in Table 2, relatively

few experiments have been able to demonstrate the formation of this species when exposed to low energy ion beams, where it typically has not been observed as a product in CO₂ ices exposed to 1.5 keV H⁺ or 2.12 keV D⁺ (Sivaraman et al. 2013) or 100 keV H⁺ ions (Raut & Baragiola 2013). However, several studies have confirmed the production of D₂CO₃ under similar circumstances, including ices exposed to 1.5 keV H⁺ ions (Brucato et al. 1997), 50–100 keV H⁺ ions (Garozzo et al. 2008), and 5 keV D₂⁺ ions (Ennis et al. 2011b). In each case, subsequent warming of the ice found that the carbonic acid remained the major ice component identified in the 185–250 K range, confirming its low volatility as recently measured by Peeters et al. (2010). The evolution of the infrared spectrum as the ice is warmed to 120, 160, 200, and 240 K is shown in Figure 2 for ease of comparison to the temperatures included by Ennis et al. (2011b). In addition, we report here for the first time the identification of D₂O during the irradiation of CO₂ ices with D⁺ ions. This species is revealed by the broad (ν₁, ν₃) absorption bands occurring at 2701 and 2741 cm⁻¹, which is in good agreement with matrix isolation studies (e.g., Engdahl et al. 2003). This species was previously identified in the experiments of Ennis et al. (2011b) after the CO₂ matrix had sublimated; in the present experiments this enables the (ν₂) band at 1177 cm⁻¹ to become visible until approximately 150 K. We were unable to identify deuterated formaldehyde (D₂CO), deuterated formic acid (DCOOD), which are both commonly identified in irradiated mixed H₂O:CO₂ ices (Pilling et al. 2010); the latter (formic acid) was also previously reported in CO₂ ices exposed to H⁺ ions (Bisschop et al. 2007). In addition, we could not unambiguously determine any potential intermediate radical or ion species toward the production of any deuterated species aside from the D₂-water and D₂-carbonic acid features, although these species may overlap with the spectral signatures of the products already identified.

3.3. Changes Observed During Warming of the Ice

Coinciding with the infrared spectra of the processed ices shown in Figure 2, Figure 3 shows the temporal evolution of

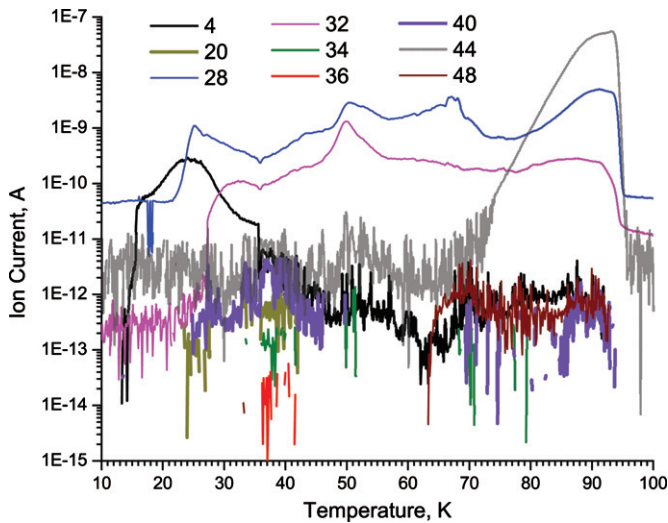


Figure 4. Ions monitored by the QMS during the sublimation of the irradiated ice from 10 to 100 K using an emission current of 0.3 mA on the ionizing filament of the QMS. The profiles of species corresponding to the D_2^+ ($m/z = 4$; black line), D_2O^+/Ar^{2+} ($m/z = 20$; olive line), CO^+ ($m/z = 28$; blue line), D_2CO^+/O_2^+ ($m/z = 32$; magenta line), D_3CO^+/DO_2^+ ($m/z = 34$; green line), $CD_3OD^+/D_2O_2^+$ ($m/z = 36$; red line), Ar^+ ($m/z = 40$; violet line), CO_2^+ ($m/z = 44$; gray line), and $DCOOD^+/O_3^+$ ($m/z = 48$; burgundy line) are shown.

(A color version of this figure is available in the online journal.)

the relative column densities for the species identified during the warm-up procedure. As the species are sublimated from the ice, it is typically possible to detect them via the QMS, as shown in Figure 4. As soon as the heating program is initiated, the column densities of both CO and $CO_3(C_{2v})$ are seen to decrease slowly, until CO sublimates from the ice at approximately 50 K, whereby the amount of $CO_3(C_{2v})$ within the ice also drops dramatically. However, it is unclear whether this species is sublimating or being broken down in the warmed ice environment. Analysis of the relative lattice band contributions of the CO_2 component indicates that a change in ice morphology at ~ 50 K is unlikely to generate additional CO_2 or O_3 , but instead influences the band strengths of these species. O_3 remains stable within the CO_2 matrix until approximately 65 K, where it begins to sublimate from the ice. The CO_2 matrix itself gradually dissipates over 55–85 K, until it begins to rapidly sublimate until the bulk CO_2 ice is no longer detectable by 94 K. As can be seen from Figure 2, (ν_3) absorption reveals that a small amount of CO_2 remains trapped in the residual ice.

The sublimation of D_2O over the period of 150–180 K, as shown in Figure 3(b), is in excellent agreement with the previous studies of Bennett et al. (2014) for the production of D_2O in O_2 ices exposed to 5 keV D^+ ions. Note that as the CO_2 sublimates at approximately 85–95 K, there is a pronounced change in the intensities of both the D_2O and D_2CO_3 bands; hence for the period beyond 100 K, absorption coefficients more appropriate to the pure ices are used in Figure 3(b). The sublimation behavior of D_2O also reveals that approximately a third of the band area remains beyond 180 K, which is attributed to the (ν_1, ν_9) absorption of D_2CO_3 . The behavior of D_2CO_3 is consistent with previous studies (e.g., Jones et al. 2014a, 2014b) where it remains in the ice until 250 K (references from Table 2). Note that the detection of the parent peak for the D_2CO_3 molecular ion was not previously reported from QMS experiments of mixed ices containing the species (e.g., Zheng & Kaiser 2007), and

that even the sublimed pure D_2CO_3 ice does not exhibit a strong parent signal in the QMS (Jones et al. 2014a, 2014b). This may be in part due to the ease with which the monomer decomposes into water and carbon dioxide in the gas phase, a process known to be facilitated by the presence of water (see Bernard et al. 2011, 2013).

The $CO_3(C_{2v}; \nu_{\text{fermi}})$ along with the $CO_3(D_{3h}; \nu_1/\nu_2)$, $CO_4(\nu_1)$, $CO_5(\nu_1)$, and $CO_6(\nu_1)$ all display similar characteristics during the heating of the ice. They remain present past the point where CO_2 sublimates at approximately 90 K before slowly sublimating until their absorption bands are no longer visible within the ice, by approximately 200 K (Figure 2). Note that the sublimation temperatures reported here are slightly above those previously reported for these species. Jamieson et al. (2007a) state that CO_4 was observed until 120 K, where it was assumed to decay into CO_2 and O_2 based on calculations by Elliot & Boldyrev (2005). Similarly, Jamieson et al. (2007b) reported that CO_5 remained in the ice until 106 K before decomposing, possibly to CO and two O_2 molecules (Elliot & Boldyrev 2005). Although CO_6 is not thought to be stable above 60 K, large variations have been observed in its band intensity during the heating of CO_2 ices (Jamieson et al. 2008).

The QMS signals recorded over the temperature range of 10–100 K are shown in Figure 4. The CO_2^+ ($m/z = 44$; gray line) matrix begins to sublimate at around 65–70 K, reaching a maximum at 94 K, and is not really detectable past 97 K. D_2^+ ($m/z = 4$; black line) is seen sublimating from 15–35 K and peaks at 24 K. CO^+ ($m/z = 28$; blue line) starts to sublimate around 23 K, but comes off in four separate steps: the first over the range of 23–35 K may be associated with the sublimation of CO, with the second perhaps due to morphological changes in the ice, which seems to peak at around 45–55 K (the same time that CO and $CO_3(C_{2v})$ were seen to drop in the infrared). The third seems to peak around 65 K and is likely associated with the release of O_3^+ ($m/z = 48$; burgundy line), and the fourth is over the same period as the sublimation of CO_2 itself. The release of O_2^+ ($m/z = 32$; magenta line) also seems to follow a similar pattern, with the exception that this species starts sublimating at a slightly higher temperature (28 K); however, it seems to be most pronounced around 45–55 K and less prominent during the release of O_3 around 65 K. This is surprising because O_2^+ is a known fragment of O_3 generated during the electron bombardment in the ionizing region of the QMS (Bennett & Kaiser 2005). Although it is difficult to observe in the infrared, the production of O_2 within irradiated CO_2 ices has been verified by Raman spectroscopy (Bennett et al. 2013a). However, it is also possible that the signal at $m/z = 32$ could also have contributions from D_2CO^+ . Indeed, there are also trace signals suggesting the formation of related species, CD_3OD^+ (or $D_2O_2^+$; $m/z = 36$; red line), and D_3CO^+ (or DO_2^+ ; $m/z = 34$; light green line) is identified between 35–42 K; the latter is additionally observed around 45–55 K coincident with the $m/z = 32$ peak, which is much lower than the sublimation temperature of methanol typically observed over 141–152 K (Bennett et al. 2007). That these species were not detected in the infrared spectrum is consistent due to the fact that the sensitivity is higher in the QMS. The peak associated with O_3^+ ($m/z = 48$; burgundy line) observed over the range of 65–94 K could potentially have contributions from $DCOOD^+$, which is of the same mass—the hydrogenated counterpart was previously observed in CO_2 ices exposed to H^+ ions (Bisschop et al. 2007). Although it is possible that D_2O^+ ($m/z = 20$; olive line) was detected over the range of 24–28 and 35–42 K, there was also

Table 3
Infrared Intensities (A-values) Used in This Study

Species	Band Position	Carrier	A-value (cm molecule ⁻¹)	Reference
CO ₂	3709	CO ₂ ($\nu_1 + \nu_3$)	1.4 × 10⁻¹⁸	Gerakines et al. (1995)
	3601	CO ₂ ($2\nu_2 + \nu_3$)	4.5 × 10 ⁻¹⁹	Gerakines et al. (1995)
D ₂ O	2701, 2741	D ₂ O (ν_1, ν_3)	6.2 × 10^{-18a} , 1.3 × 10 ^{-16 b}	Bennett et al. (2014)
CO	2139	CO (ν_1)	1.1 × 10 ⁻¹⁸	Gerakines et al. (1995)
CO ₃ (C _{2v})	2044	CO ₃ (C _{2v} ; ν_1)	8.9 × 10 ⁻¹⁷	Bennett et al. (2004)
CO ₄	1943	CO ₄ (ν_1)	1.0 × 10 ⁻¹⁶	Jamieson et al. (2007a)
CO ₅	1916	CO ₅ (ν_1)	8.0 × 10 ^{-17 c}	Jamieson et al. (2007b)
CO ₆	1893	CO ₆ (ν_1)	5.5 × 10 ^{-17c}	Jamieson et al. (2008)
D ₂ CO ₃	1729	D ₂ CO ₃ (ν_2)	1.0 × 10^{-16a} , 3.3 × 10 ^{-16 b,d}	Gerakines et al. (2000)
	1385	D ₂ CO ₃ (ν_{10})	8.4 × 10 ^{-17 a,e} , 3.3 × 10 ^{-16 b,d}	
CO ₃ (D _{3h})	1169, 1189sh	CO ₃ (D _{3h} ; ν_1/ν_2)	1.2 × 10 ⁻¹⁷	Bennett et al. (2004)
O ₃	1042	O ₃ (ν_3)	1.5 × 10 ⁻¹⁸	Bennett & Kaiser (2005)

Notes. Where multiple values are given, the values in bold represent those used to derive the column densities for the temporal profiles of each species during irradiation.

^a Value used during the irradiation period and until the CO₂ ice sublimated.

^b Value used after the CO₂ ice sublimated.

^c B3LYP/6–311G(d) values were used.

^d Value taken from Garozzo et al. (2008), but rescaled based on the relative intensity of the deuterated version as calculated by Wight & Boldyrev (1995) using the procedure from Bennett et al. (2014).

^e This A-value is taken from the scaled from relative area of this band from that of the peak at 1729 cm⁻¹, which was taken as the value from Gerakines et al. (2000).

the detection of a stronger peak that may be associated with Ar⁺ ($m/z = 40$); therefore, this detection in itself is not definitive. Note that no signal for D₂CO₃⁺ ($m/z = 64$) was monitored; however this species has not been detected in mixed CO₂:H₂O ices where carbonic acid was produced by electron irradiation (Zheng & Kaiser 2007; Jones et al. 2014a). This species has been shown to be stable at 185 K (Garozzo et al. 2008) and was found to sublime at around 260 K when pure carbonic acid samples were heated (Jones et al. 2014a; even here, the molecular ion is only weakly detected).

3.4. Chemical Modeling of Reactions Induced by Irradiation

Here, we attempt to determine some of the underlying reaction mechanisms to account for how the observed species might actually be synthesized during the irradiation process. To illustrate some of the potential pathways, four general schemes were developed (A–D) to fit the temporal column densities of species that are observed to change during irradiation. Minor modifications to some of these models (A2–A4 and D2) were included to show how certain variables influence them. The spectra were typically averaged over an hour of data in order to improve the signal to noise and reduce the total number of spectra required for analysis and input into the kinetic model. A deconvolution routine was implemented to fit single or multiple Gaussians to the data along with an optional linear baseline subtraction. The absorption bands used for the calculation of column densities for each species are listed in Table 3. Systems of up to 22 coupled differential equations from those listed in Table 4 were solved numerically by an iterative procedure for each system (Frenklach 1984; Frenklach et al. 1992, 2007). The resulting fits of each model are shown in Figure 5, with the derived rate constants listed in Table 4. The associated error in reproducing the experimental column densities of each species

is listed in Table 5. In each model, the source of D⁺ ions, and hence the total D atoms available, was determined by the fluence to be $8.7 \times 10^{10} \text{ s}^{-1}$. The TRIM calculations demonstrated that >99.9% of the D⁺ ions should come to rest within 500 nm of the CO₂ ice ($6.37 \times 10^{17} \text{ molecules cm}^{-2}$), therefore this was taken as the ice thickness in all models. Reactions R1–R7 and R9–R14 are bond cleavages, which typically require a few eV of energy. Reaction R8 is an isomerization, and the barrier for this process was calculated as 18.4 kJ mol⁻¹ (Bennett et al. 2004). Reactions R15 through R33 are either representative of addition, recombination, insertion, or abstraction reactions. In most instances, the reactions chosen here are either barrierless or have small enough entrance barriers to be overcome by the reactants in the ice. The production of these species by radiolysis can generate species that are not in thermal equilibrium with the ice—they may be translationally, rotationally, vibrationally, and/or electronically hot, which would allow these reactions to proceed efficiently under such conditions, even with barriers. As a result, the notation in Table 4 neglects the potential involvement of excited states even though they may be involved in the stated reactions. The rate constant for the addition of atomic oxygen to molecular oxygen to form ozone (R17) is fixed at a value of $1.18 \times 10^{-22} \text{ cm}^2 \text{ molecules}^{-1} \text{ s}^{-1}$ in line with our previous study (Bennett et al. 2014), which also served to analyze several alternative pathways for the generation of both D₂-water and O₃ (such as the choice of R3 over that of a competing reaction pathway $\text{O}_3 + \text{O} \rightarrow 2\text{O}_2$). For most models, the formation of D₂O was thought to occur via the successive addition of D atoms to O, to initially form OD, then again to form the D₂-water molecule, as the pathways to the species were also investigated at depth in the previous investigation.

A general outline of the different reaction schemes adopted in models A–D2 is shown schematically in Figure 6. In models A–A4, the formation of D₂CO₃ was tested to occur via the

Table 4
Summary of Reaction Rates Derived for Each Considered Reaction Scheme Labeled as Models A–D2

No.	Reaction	Rate ^a							
		Model A	Model A2	Model A3	Model A4	Model B	Model C	Model D	Model D2
1	CO ₂ → CO + O	1.98 × 10 ⁻⁵	1.85 × 10 ⁻⁵	2.65 × 10 ⁻⁵	1.82 × 10 ⁻⁵	2.15 × 10 ⁻⁵	1.85 × 10 ⁻⁵	2.11 × 10 ⁻⁵	1.60 × 10 ⁻⁵
2	O ₂ → O + O	1.47 × 10 ⁻⁵	2.26 × 10 ⁻⁵	1.62 × 10 ⁻⁵	9.86 × 10 ⁻⁶	1.60 × 10 ⁻⁵	1.51 × 10 ⁻⁵	8.59 × 10 ⁻⁵	6.45 × 10 ⁻⁵
3	O ₃ → O ₂ + O	2.33 × 10 ⁻³	2.37 × 10 ⁻³	2.33 × 10 ⁻³	2.34 × 10 ⁻³	2.12 × 10 ⁻³	2.06 × 10 ⁻³	1.04 × 10 ⁻³	2.15 × 10 ⁻³
4	CO ₃ (C _{2v}) → CO ₂ + O	2.97 × 10 ⁻⁴	...	1.59 × 10 ⁻⁴	1.81 × 10 ⁻³	2.92 × 10 ⁻⁴	6.17 × 10 ⁻²	7.80 × 10 ⁻²	5.66 × 10 ⁻⁴
5	CO ₃ (C _{2v}) → CO + O ₂	...	4.39 × 10 ⁻⁴
6	CO ₃ (D _{3h}) → CO ₂ + O	6.85 × 10 ⁻⁶	...	7.78 × 10 ⁻⁶	5.24 × 10 ⁻⁹	6.66 × 10 ⁻⁶	7.09 × 10 ⁻⁶	1.60 × 10 ⁻⁹	1.39 × 10 ⁻⁸
7	CO ₃ (D _{3h}) → CO + O ₂	...	7.55 × 10 ⁻⁶
8	CO ₃ (C _{2v}) → CO ₃ (D _{3h})	3.87 × 10 ⁻¹⁰
9	CO ₄ → CO ₂ + O ₂	3.49 × 10 ⁻⁹	1.76 × 10 ⁻⁶	2.17 × 10 ⁻⁶	6.83 × 10 ⁻⁵	1.90 × 10 ⁻⁸	7.72 × 10 ⁻¹¹	7.50 × 10 ⁻⁸	5.58 × 10 ⁻⁷
10	CO ₅ → CO + O ₂ + O ₂	4.98 × 10 ⁻⁵	3.44 × 10 ⁻⁵	3.04 × 10 ⁻⁵	3.07 × 10 ⁻⁵	4.83 × 10 ⁻⁵	4.16 × 10 ⁻⁵	5.17 × 10 ⁻⁵	4.81 × 10 ⁻⁵
11	CO ₆ → CO ₂ + O ₂ + O ₂	1.61 × 10 ⁻⁵	1.60 × 10 ⁻⁵	1.58 × 10 ⁻⁵	1.98 × 10 ⁻⁵	1.33 × 10 ⁻⁵	1.65 × 10 ⁻⁵	2.08 × 10 ⁻⁵	2.15 × 10 ⁻⁵
12	D ₂ O → OD + D	8.01 × 10 ⁻⁶	3.14 × 10 ⁻¹⁰	7.33 × 10 ⁻⁷	5.12 × 10 ⁻¹⁰	7.74 × 10 ⁻⁷	1.92 × 10 ⁻⁸	1.54 × 10 ⁻⁹	7.91 × 10 ⁻⁹
13	D ₂ CO ₃ → DOCO + OD	1.29 × 10 ⁻⁵	2.86 × 10 ⁻⁹	5.15 × 10 ⁻⁹	2.56 × 10 ⁻⁹	1.00 × 10 ⁻⁵
14	D ₂ CO ₃ → DCO ₃ + D	4.26 × 10 ⁻⁶	2.73 × 10 ⁻⁶	1.09 × 10 ⁻⁵	...
15	CO + O → CO ₂	7.57 × 10 ⁻²²	8.61 × 10 ⁻²²	1.07 × 10 ⁻²¹	7.47 × 10 ⁻²²	8.16 × 10 ⁻²²	6.44 × 10 ⁻²²	5.02 × 10 ⁻²²	5.74 × 10 ⁻²²
16	O + O → O ₂	1.25 × 10 ⁻²²	8.81 × 10 ⁻²⁶	1.57 × 10 ⁻²²	1.09 × 10 ⁻²²	1.17 × 10 ⁻²²	8.56 × 10 ⁻²³	6.53 × 10 ⁻²³	3.57 × 10 ⁻²²
17	O ₂ + O → O ₃ ^b	1.18 × 10 ⁻²⁰							
18	CO ₂ + O → CO ₃ (C _{2v})	1.98 × 10 ⁻²³	3.19 × 10 ⁻²³	1.13 × 10 ⁻²³	1.28 × 10 ⁻²²	1.93 × 10 ⁻²³	3.71 × 10 ⁻²¹	3.17 × 10 ⁻²¹	3.53 × 10 ⁻²³
19	CO ₂ + O → CO ₃ (D _{3h})	4.93 × 10 ⁻²⁵	5.08 × 10 ⁻²⁵	4.81 × 10 ⁻²⁵	6.01 × 10 ⁻²⁵	4.64 × 10 ⁻²⁵	4.29 × 10 ⁻²⁵	5.34 × 10 ⁻²⁵	7.95 × 10 ⁻²⁵
20	CO ₃ (C _{2v}) + O → CO ₄	3.78 × 10 ⁻²³	4.30 × 10 ⁻²³	3.92 × 10 ⁻²³	2.98 × 10 ⁻²³	3.88 × 10 ⁻²³	3.36 × 10 ⁻²³	4.00 × 10 ⁻²³	6.00 × 10 ⁻²³
21	CO ₃ (D _{3h}) + O → CO ₄	4.19 × 10 ⁻²³	1.87 × 10 ⁻²³	1.39 × 10 ⁻²³	1.92 × 10 ⁻²²	3.44 × 10 ⁻²³	2.63 × 10 ⁻²³	2.30 × 10 ⁻²⁴	...
22	CO ₄ + O → CO ₅	7.06 × 10 ⁻²²	5.74 × 10 ⁻²²	4.95 × 10 ⁻²²	5.21 × 10 ⁻²²	6.70 × 10 ⁻²²	5.55 × 10 ⁻²²	4.61 × 10 ⁻²²	6.64 × 10 ⁻²²
23	CO ₅ + O → CO ₆	9.23 × 10 ⁻²³	9.99 × 10 ⁻²³	9.73 × 10 ⁻²³	1.18 × 10 ⁻²²	7.81 × 10 ⁻²³	8.61 × 10 ⁻²³	7.13 × 10 ⁻²³	1.12 × 10 ⁻²²
24	O + D → OD	2.22 × 10 ⁻¹⁹	1.78 × 10 ⁻¹⁹	9.50 × 10 ⁻¹⁸	3.90 × 10 ⁻¹⁸	5.68 × 10 ⁻¹⁹	3.32 × 10 ⁻¹⁸
25	O ₃ + D → O ₂ + OD	1.06 × 10 ⁻¹⁹
26	CO ₂ + D → CO + OD	1.50 × 10 ⁻²⁰
27	D + OD → D ₂ O	6.28 × 10 ⁻¹⁶	1.99 × 10 ⁻¹⁵	5.45 × 10 ⁻¹⁶	4.90 × 10 ⁻¹⁷	1.29 × 10 ⁻¹⁵	1.07 × 10 ⁻¹⁵	4.36 × 10 ⁻¹⁷	1.69 × 10 ⁻¹⁶
28	CO ₂ + D → DOCO	2.99 × 10 ⁻²⁰	2.28 × 10 ⁻²⁰	1.32 × 10 ⁻²¹	1.34 × 10 ⁻²⁰
29	CO ₂ + OD → DCO ₃	1.98 × 10 ⁻²²
30	CO ₃ (C _{2v}) + D → DCO ₃	1.07 × 10 ⁻¹⁶
31	CO ₃ (D _{3h}) + D → DCO ₃	3.74 × 10 ⁻¹⁷	1.41 × 10 ⁻¹⁶
32	DOCO + OD → D ₂ CO ₃	1.47 × 10 ⁻²⁰	6.60 × 10 ⁻²⁰	1.78 × 10 ⁻¹⁹	2.83 × 10 ⁻²¹	8.66 × 10 ⁻¹⁸
33	DCO ₃ + D → D ₂ CO ₃	6.19 × 10 ⁻¹⁸	4.71 × 10 ⁻¹⁸	2.35 × 10 ⁻¹⁸	...

Notes.

^a Unimolecular reactions (A→B) are in units of s⁻¹; bimolecular reactions (A + B→C) are in units of cm² molecules⁻¹ s⁻¹; note that the typical units for the rate of a bimolecular reaction of cm³ molecules⁻¹ s⁻¹ are not applicable here, as our concentrations are presented in terms of column densities (molecules cm⁻²), rather than concentration (molecules cm⁻³).

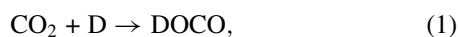
^b The rate constant for R17 (O₂ + O→O₃; italicized) was fixed for each model during the iterative fitting procedure, for ease of comparison.

Table 5
Summary of Errors of Each of the Models to the Experimentally Derived Column Densities for Species Monitored Throughout the Experiment

Error ^a	Model A	Model A2	Model A3	Model A4	Model B	Model C	Model D	Model D2
CO ₂	0.0794	0.0918	0.1059	0.0560	0.0825	0.0711	0.1376	0.1030
O ₃	0.6563	0.6730	0.5396	0.7838	0.7330	0.8822	1.2211	1.1658
CO	0.0277	0.0617	0.0352	0.0550	0.0173	0.0233	0.1905	0.1454
CO ₃ (C _{2v})	0.9071	0.8462	1.0093	0.7107	0.8562	0.4424	0.8755	1.0701
CO ₃ (D _{3h})	0.7791	0.5951	0.6234	1.0610	0.6988	0.7392	1.0930	1.0059
CO ₄	0.2266	0.5205	0.6350	0.1592	0.3081	0.2948	0.5792	0.6323
CO ₅	0.7739	0.8586	1.0573	1.0177	0.8323	0.9292	0.9664	0.9744
CO ₆	2.7019	2.7565	2.5943	2.4797	2.7345	2.4577	2.3025	2.2981
D ₂ O	0.8448	0.8588	1.8748	0.8992	0.9713	1.2136	1.0443	1.0590
D ₂ CO ₃	0.1583	0.1782	0.1245	0.1321	0.1023	0.1157	0.1005	0.1012
Total	7.1553	7.4405	8.5992	7.3545	7.3363	7.1693	8.5107	8.5552

Note. ^a Normalized residual sum-of-squares.

following reactions:



Although no evidence could be found for either the *cis*- or *trans*-form of the DOCO radical, for which the strongest absorption occurs in the range of 1773–1825 cm⁻¹ (Bennett et al. 2011), this species was identified in mixed CO₂:H₂O ices exposed to 5 keV electrons in experiments performed by Zheng &

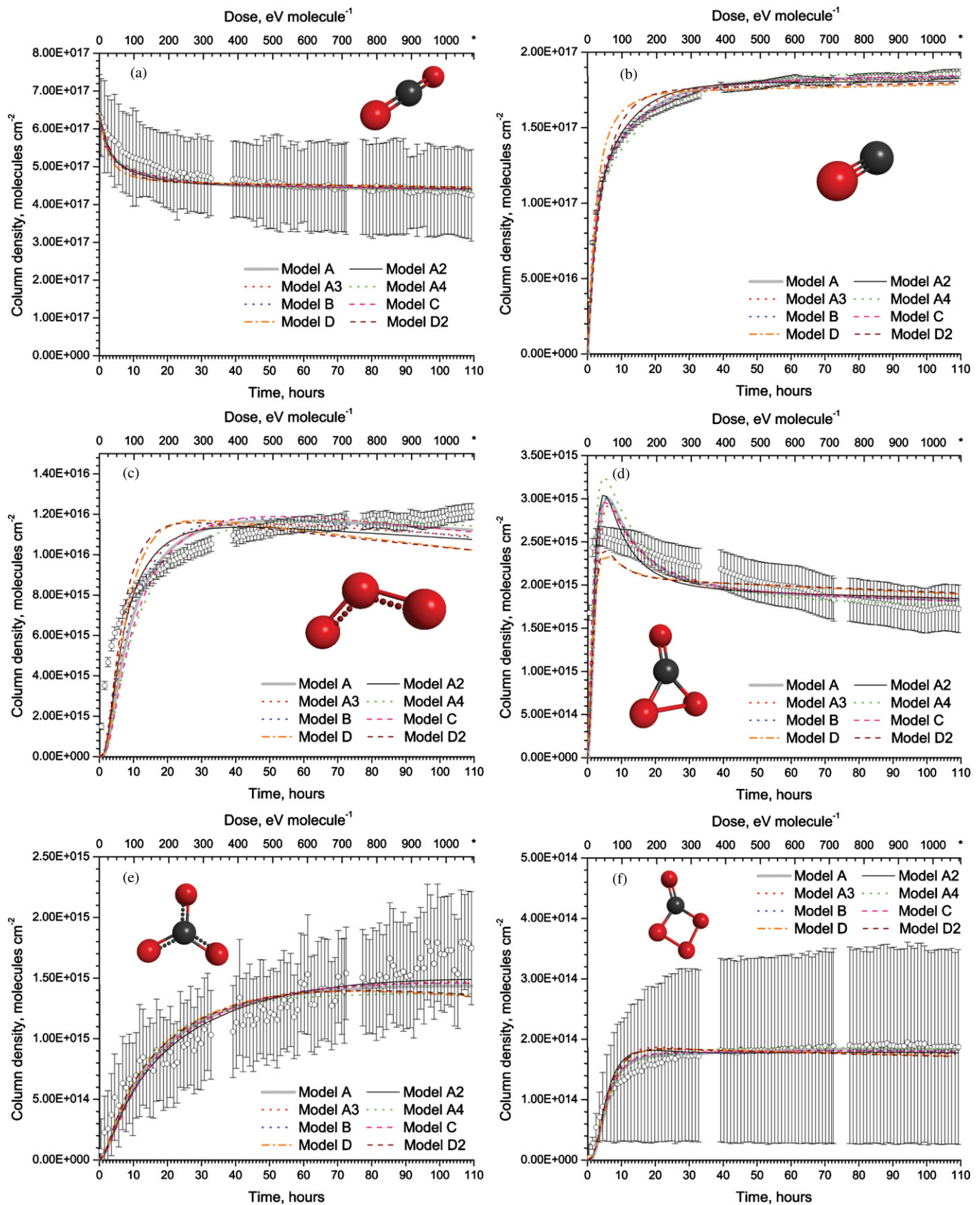


Figure 5. Temporal profiles of the column densities during the irradiation period for (a) CO₂, (b) CO, (c) O₃, (d) CO₃(C_{2v}), (e) CO₃(D_{3h}), (f) CO₄, (g) CO₅, (h) CO₆, (i) D₂O, and (j) D₂CO₃. The kinetic fits are also shown for each species according to the reaction schemes listed in Table 4. (A color version of this figure is available in the online journal.)

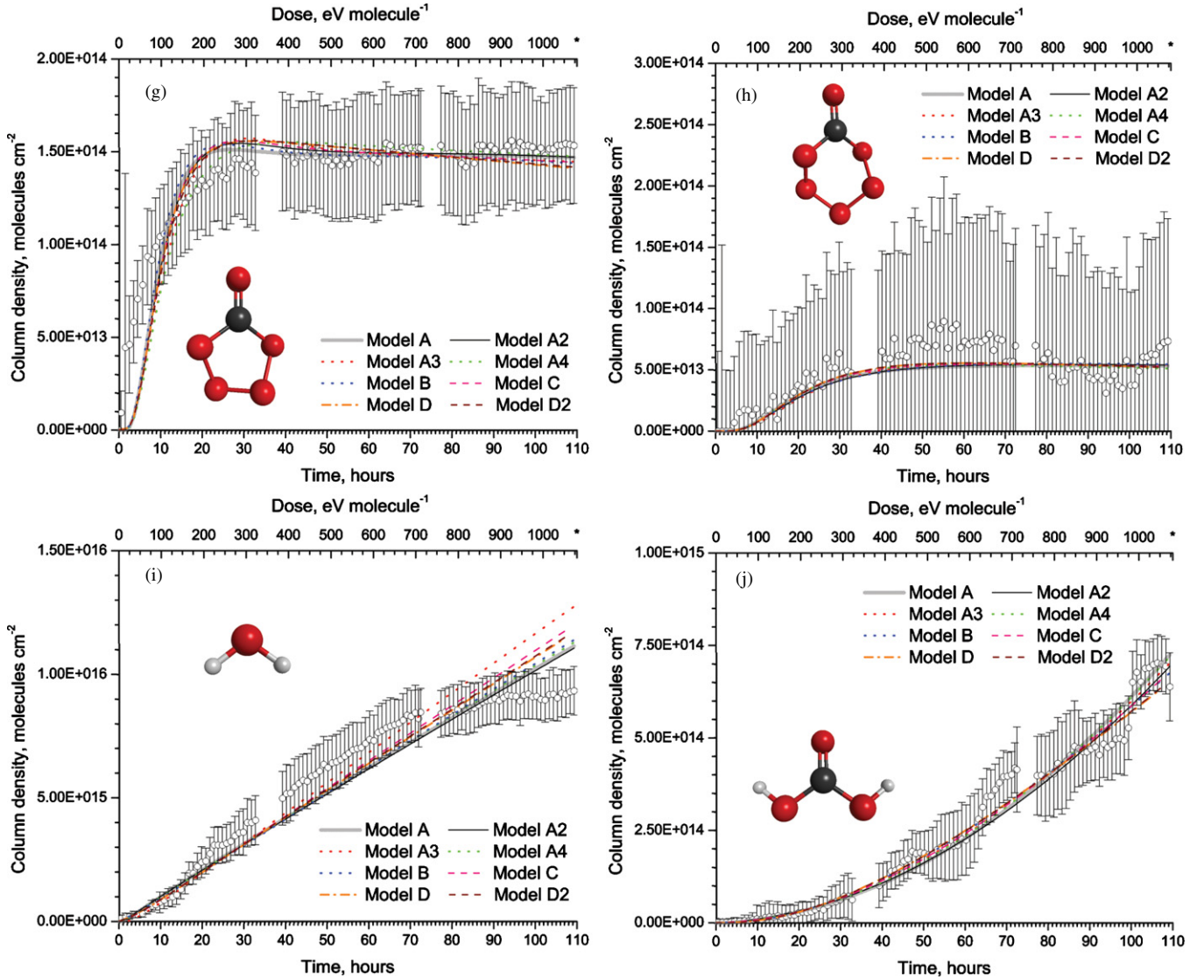


Figure 5. (Continued)

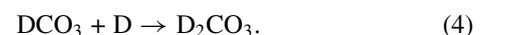
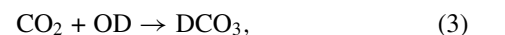
Kaiser (2007). Here, the authors proposed that the pathway through reactions (1) and (2) would be the most likely to form D_2CO_3 in their ices. The approximate 1 eV barrier for reaction (1) (Song et al. 2006; Bennett & Kaiser 2007) could be overcome by the energy supplied to our impinging D^+ ions (and by analogy, could also be experienced by CO_2 ices interacting with the solar wind). Reaction (2) is representative of a radical–radical reaction and should proceed with no reaction barrier, even within low temperature environments.

Note that most of the dissociation pathways considered here lead to more stable products. However, these are not the only possible pathways and it is prudent to briefly discuss the variations that can be induced by not adhering to this rule, which were typically negligible. Model A2 features an alternative scenario where the CO_3 isomers are dissociated to form $CO + O_2$ (reactions R5 and R7), rather than $CO_2 + O$ (reactions R4 and R6). In this particular case, Table 5 shows that the resulting fits were better able to reproduce the experimental column densities for both CO_3 isomers, albeit the overall fits for the majority of the species had slightly larger errors.

The formation of OD can also occur by a suprathermal process known as abstraction, whereby the hot D atoms are able to abstract an oxygen atom from a previously formed molecule.

We briefly investigate two pathways where this could occur to produce the OD radical (as opposed to reaction R24) via either (1) O_3 to form OD (R25) and O_2 as shown in model A3, or (2) CO_2 to form CO and OD (R26) as depicted in model A4 (Song et al. 2006). When Bennett et al. (2014) investigated the same pathway as model A3, they noted that the combination of the low barrier for reaction R25 (~ 100 K) and the production of energetic OD radicals could potentially overcome subsequent reaction barriers. The results shown in Table 5 indicate that this model was better able to reproduce the experimentally determined column densities of both O_3 and D_2CO_3 . In model A4, the barrier for R26 is higher, ranging at around about 1 eV (Song et al. 2006), but again this is easily accessible to suprathermal H/D atoms or ions. The additional pathway leading to the destruction of CO_2 allowed for the best reproduction of the experimental CO_2 column density (Table 5).

The formation of D_2CO_3 was suggested to occur via the following reactions, which were integrated into model B:



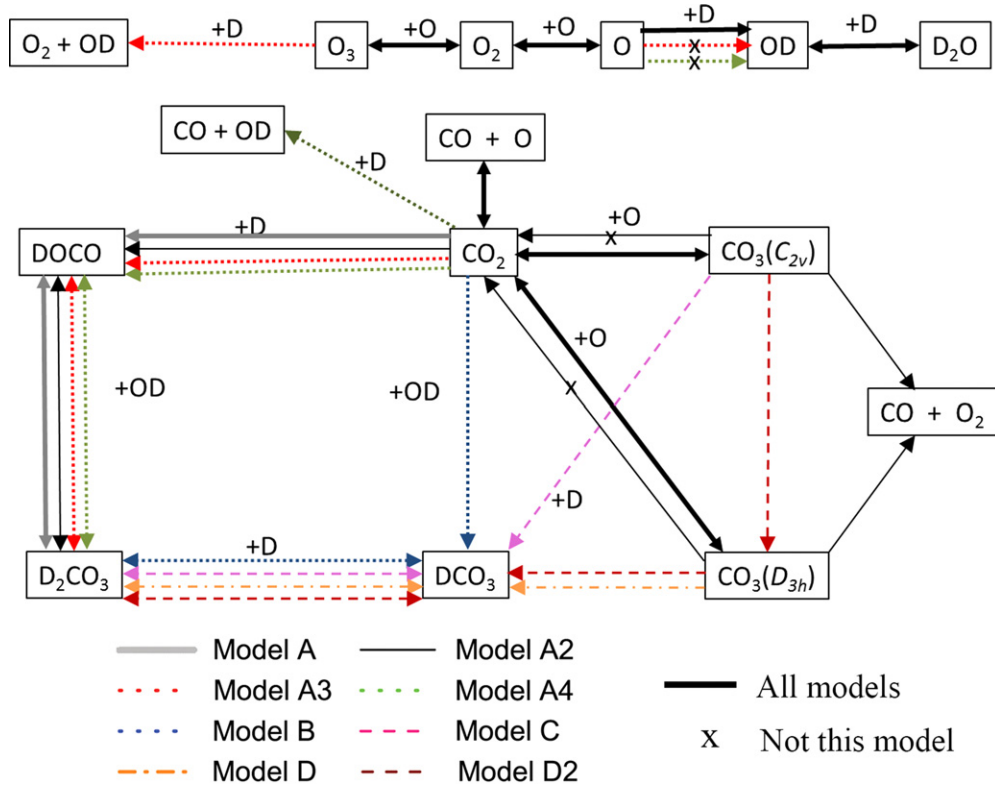
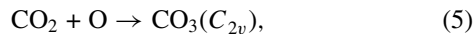


Figure 6. Summary of the alternative reaction pathways investigated by models A–D2.

(A color version of this figure is available in the online journal.)

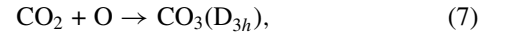
Zheng & Kaiser (2007) also considered this reaction process, but since they could not find evidence for the formation of DCO_3 as opposed to finding evidence for the formation of DOCO , they concluded reactions (1) and (2) to be the dominant pathways. However, since the vibrational modes of DCO_3 are not particularly distinct from those of D_2CO_3 , it is difficult to verify or discount the involvement of this species. The barrier for reaction (3) is 0.76 eV (Montgomery et al. 2008), with no barrier thought to occur for reaction (4). If OD is produced through reactions R24–R26, it could be energetic enough to overcome such a barrier if it is produced in close vicinity to the CO_2 molecule. Note that this reaction scheme bears many similarities to that suggested by Gerakines et al. (2000), and supported by Pilling et al. (2010), that the CO_2 could react without barrier with an OD^- species (i.e., generated here by the capture on a secondary electron generated within the ice via S_e processes; Wight & Boldyrev 1995; Leung et al. 2007). This would lead to the production of DCO_3^- , which could then form D_2CO_3 via an acid–base reaction with D^+ . The inclusion of the OD^- pathway was not omitted here because the presence of this species could not be substantiated; note that there is also some theoretical evidence that a barrier exists for this process (e.g., Iida et al. 2007). Model B was very effective in reproducing the experimentally derived column densities of CO and D_2CO_3 .

Strazzulla et al. (2005) noted that the production of carbonic acid seemed to be connected to the production of $\text{CO}_3(\text{C}_{2v})$. Therefore, the following reaction sequence was suggested to result in the formation of D_2CO_3 in model C:



followed by reaction (4), to form carbonic acid. This pathway was also considered by Ennis et al. (2011b), although chiefly on the basis that $\text{CO}_3(\text{C}_{2v})$ was the only abundant precursor identified within the CO_2 ices exposed to energetic D_2^+ ions. Unfortunately, the kinetic model was deemed beyond the scope of their analysis. Reaction (5) can occur in irradiated ices, as verified by several previous experiments (e.g., Bennett et al. 2004, 2009a, 2009b, 2010; Ennis et al. 2011b). Although a small barrier for reaction (6) should be present because it requires a bond cleavage, the only calculation we are aware of suggests that there may not be barrier for this reaction (Montgomery et al. 2008). If a barrier is present, it could be overcome because our reacting D atoms can be suprathreshold. There should be no barrier for the radical–radical reaction (6). Model C was able to account for the experimentally determined column densities very well for all species, especially the $\text{CO}_3(\text{C}_{2v})$ species.

Lastly, the alternative formation of D_2CO_3 via the other isomer, $\text{CO}_3(\text{D}_{3h})$, is investigated in the reaction schemes of models D and D2:



followed again, by reaction (4), to form carbonic acid. To our knowledge, this reaction pathway has not been suggested previously, as only the previous study of Sivaraman et al. (2013) was able to identify a $\text{CO}_3(\text{D}_{3h})$ isomer whose production was verified through the radiation of CO_2 ices (Jamieson et al. 2006). Although, as with the C_{2v} isomer, no barrier has been calculated for the reaction between the $\text{CO}_3(\text{D}_{3h})$ and D atoms (R31; Montgomery et al. 2008), one is expected to exist, and may be lower than that for the C_{2v} isomer. The formation of D_2CO_3

exclusively through the reaction of D atoms with the $\text{CO}_3(D_{3h})$ isomer, along with the exclusive production of CO_4 and higher oxide species through the reaction of the barrierless insertion of $\text{O}(^1\text{D})$ atoms with $\text{CO}_3(C_{2v})$, was considered in model D2. In addition, the conversion between the $\text{CO}_3(C_{2v})$ and $\text{CO}_3(D_{3h})$ forms was investigated by the inclusion of R8; however, this was not shown to play an important role.

4. ASTROPHYSICAL IMPLICATIONS

In summary, our studies demonstrate that the implantation of 5 keV D^+ ions into molecular CO_2 ices at 12 K leads to the production of CO , O_3 , $\text{CO}_3(C_{2v})$, $\text{CO}_3(D_{3h})$, and D2-carbonic acid as previously identified, as well as the newly identified products CO_4 , CO_5 , CO_6 , and D2-water. The kinetic models investigated suggest that multiple pathways to form D2-carbonic acid are feasible. These models represent the first kinetic models that quantitatively account for the destruction of CO_2 and production of CO , O_3 , $\text{CO}_3(C_{2v})$, $\text{CO}_3(D_{3h})$, CO_4 , CO_5 , CO_6 , D2-carbonic acid, and D2-water during the exposure of pure CO_2 ices to 5 keV D^+ ions. We also found evidence for the production of trace amounts of D2-formaldehyde (D_2CO), D4-methanol (CD_3OD), and D2-formic acid (DCOOD) in the QMS profiles of the sublimated ice post irradiation.

The TRIM calculations indicate that the 5 keV of kinetic energy from the incoming D^+ ions is partitioned primarily into the electronic (S_e) transfer processes (90%), with the remainder being transferred through nuclear (S_n) interactions with the ice. The linear energy transfer to the ice is found to be approximately 20 keV μm^{-1} . During the irradiation period, the sample was exposed to a total of $3.4 \pm 0.5 \times 10^{16}$ D^+ ions, with each bearing 5 keV of kinetic energy and exposing the ice to an estimated dose of 1080 ± 320 eV molecule $^{-1}$. These values can be used to directly compare our derived column densities to those that could be expected to evolve within astronomical ices exposed to similar doses of radiation, as has been done previously in the literature. For example, Strazzulla et al. (2005) estimated that the conditions of their experiment, which exposed a mixed $\text{CO}_2:\text{H}_2\text{O}$ ice to 2.0×10^{14} He^+ ions of 200 keV energy, would translate to 200 yr at the equivalent irradiation dose received by the Martian surface ($6000 \text{ MeV cm}^{-2} \text{ s}^{-1}$; Molina-Cuberos et al. 2001). Using a similar approach, we estimate that the total irradiation period of our experiments would correspond to approximately 900 yr of irradiation on the Martian surface, with some of the species identified, such as $\text{CO}_3(C_{2v})$ and O_3 , reaching approximately steady-state concentrations after 5%–25% of this dose. However, bear in mind that if we were instead to consider solar wind H^+ ions of energy 1.5 keV, the same amount of carbonic acid and water would be expected to be produced in approximately 270 yr. Although this time period suggests that large amounts of these species may not be detectable at the northern pole (which is transient), there would be sufficient irradiation reaching the southern poles. In addition, as noted by Strazzulla et al. (2005), it is anticipated that a number of the species produced within these experiments should be detectable either within the ices or atmosphere, most likely as the northern pole sublimates. Our QMS detections indicate that H_2CO , CH_3OH , and HCOOH could also be detectable in the atmosphere by MAVEN, to support a previous suggestion by Wu et al. (2011). The production of volatile species such as O_2 and CO could additionally explain some of the unusual terrain observed at the poles associated with the sublimation of submerged CO_2 ice (e.g., Hansen et al. 2010); their icy

origin before was detected as minor constituents of the Martian atmosphere (0.13% and 0.08%, respectively).

Similarly, Strazzulla & Johnson (1991) estimated that the outer 0.5 m of a comet surface is exposed to an irradiation dose of approximately 600 eV molecule $^{-1}$, which is of the same order as the dose applied in these studies. In addition, the production of larger CO_x ($x = 3\text{--}6$) produced from the irradiation of CO_2 ices, as well as species produced from the irradiation of CO ices (such as large chain molecules as C_6O ; Bennett et al. 2008), could serve as extended sources for CO and CO_2 observed for comets (e.g., Cottin & Fray 2008; Reach et al. 2013). These studies are also relevant to the icy moons of the gas and ice giants in the solar system. For example, it was recently shown that when carbonic acid produced from irradiation is annealed to release the precursor molecules and subsequently re-irradiated by 5 keV electrons, the resulting CO_2 band profile matched very well that observed on Jupiter's moon, Callisto (Hage et al. 1998; Jones et al. 2014b). The fact that water can be produced from the irradiation of pure CO_2 ices is often overlooked, yet this could have important consequences within these astronomical environments. In addition, these experiments also have implications for the formation of $\text{OH}/\text{H}_2\text{O}$ on the lunar surface. Since hot-atom reactions are thought to cleave Si–O bonds in a similar manner, hot H atoms are able to insert and react with the oxygen (and silicon) within the silicate materials (e.g., Starukhina 2006; Clark 2009).

This material was based upon work supported by the National Aeronautics and Space Administration (NASA Astrobiology Institute under Cooperative Agreement No. NNA09DA77A issued through the Office of Space Science).

REFERENCES

- Bennett, C. J., Brotton, S. J., Jones, B. M., et al. 2013a, *AnaCh*, 85, 5659
 Bennett, C. J., Chen, S.-H., Sun, B.-J., Chang, A. H. H., & Kaiser, R. I. 2007, *ApJ*, 600, 1588
 Bennett, C. J., Ennis, C. P., & Kaiser, R. I. 2014, *ApJ*, 782, 63
 Bennett, C. J., Hama, T., Kim, Y. S., Kawasaki, M., & Kaiser, R. I. 2011, *ApJ*, 727, 27
 Bennett, C. J., Jamieson, C., Mebel, A. M., & Kaiser, R. I. 2004, *PCCP*, 6, 735
 Bennett, C. J., Jamieson, C. S., & Kaiser, R. I. 2008, *P&SS*, 56, 1181
 Bennett, C. J., Jamieson, C. S., & Kaiser, R. I. 2009a, *PCCP*, 11, 4210
 Bennett, C. J., Jamieson, C. S., & Kaiser, R. I. 2009b, *ApJS*, 182, 1
 Bennett, C. J., Jamieson, C. S., & Kaiser, R. I. 2010, *PCCP*, 12, 4032
 Bennett, C. J., Jamieson, C. S., Osamura, Y., & Kaiser, R. I. 2005, *ApJ*, 624, 1097
 Bennett, C. J., & Kaiser, R. I. 2005, *ApJ*, 635, 1362
 Bennett, C. J., & Kaiser, R. I. 2007, *ApJ*, 660, 1289
 Bennett, C. J., Pirim, C., & Orlando, T. M. 2013b, *Chem. Rev.*, 113, 9086
 Bernard, J., Huber, R., Liedl, K. R., Grothe, H., & Loerting, T. 2013, *JChS*, 135, 7732
 Bernard, J., Seidl, M., Kohl, I., et al. 2011, *Angew. Chem. Int. Ed.*, 50, 1939
 Bibring, J.-P., Langevin, Y., Poulet, F., et al. 2004, *Natur*, 428, 627
 Bisschop, S. E., Fuchs, G. W., van Dishoeck, E. F., & Linnartz, H. 2007, *A&A*, 474, 1061
 Brown, R. H., Clark, R. N., & Buratti, B. J. 2006, *Sci*, 311, 1425
 Brucato, J. R., Palumbo, M. R., & Strazzulla, G. 1997, *Icar*, 125, 135
 Buratti, B. J., Cruikshank, D. P., Brown, R. H., et al. 2005, *ApJL*, 622, L149
 Cahill, J. E. 1977, *JChPh*, 66, 4847
 Carlson, R. W. 1999, *Sci*, 283, 820
 Chaban, G. M., Bernstein, M., & Cruikshank, D. P. 2007, *Icar*, 187, 592
 Clark, R. N. 2009, *Sci*, 326, 562
 Clark, R. N., Brown, R. H., Jaumann, R., et al. 2005, *Natur*, 435, 66
 Clark, R. N., Carlson, R., Grundy, W., & Noll, K. 2013, in *The Science of Solar System Ices*, ed. M. S. Guidipati & J. Castrillo-Rogez (Astrophysical and Space Science Library, Vol 356; New York: Springer), 3
 Cottin, H., & Fray, N. 2008, *SSRv*, 138, 179
 Cruikshank, D. P., Meyer, A. W., Brown, R. H., et al. 2010, *Icar*, 206, 561
 Cruikshank, D. P., Roush, T. L., Owen, T. C., et al. 1993, *Sci*, 261, 742

- DelloRusso, N., Khanna, R. K., & Moore, M. H. 1993, *JGR*, **98**, 5505
- Elliot, B. M., & Boldyrev, A. I. 2005, *JPCA*, **109**, 3722
- Engdahl, A., Karlström, G., & Nelander, B. 2003, *JChPh*, **118**, 7797
- Ennis, C. P., Bennett, C. J., & Kaiser, R. I. 2011a, *PCCP*, **13**, 9469
- Ennis, C., Bennett, C. J., & Kaiser, R. I. 2011b, *ApJ*, **733**, 79
- Frenklach, M. 1984, *CoFl*, **58**, 69
- Frenklach, M., Packard, A., & Feeley, R. 2007, in *Modeling of Chemical Reactions*, ed. R. W. Carr (Elsevier Series Comprehensive Chemical Kinetics, Vol. 42; Amsterdam: Elsevier), 243
- Frenklach, M., Wang, H., & Rabinowitz, M. J. 1992, *PrECS*, **18**, 47
- Garozzo, M., Fulvio, D., Gomis, O., Palumbo, M. R., & Strazzulla, G. 2008, *P&SS*, **56**, 1300
- Gerakines, P. A., Moore, M. H., & Hudson, R. L. 2000, *A&A*, **357**, 793
- Gerakines, P. A., Schutte, W. A., & Ehrenfreund, P. 1996, *A&A*, **312**, 289
- Gerakines, P. A., Schutte, W. A., Greenberg, J. M., & van Dishoeck, E. F. 1995, *A&A*, **296**, 810
- Grundy, W. M., Young, L. A., Spencer, J. R., et al. 2006, *Icar*, **184**, 543
- Grundy, W. M., Young, L. A., & Young, E. F. 2003, *Icar*, **162**, 223
- Hage, W., Liedl, K. R., Hallbrucker, A., & Mayer, E. 1998, *Sci*, **279**, 1332
- Hansen, C. J., Thomas, N., Portyankina, G., et al. 2010, *Icar*, **205**, 283
- Hansen, G. B. 1999, *JGRE*, **104**, 16471
- Hansen, G. B. 2013, *Icar*, **225**, 869
- Hibbitts, C. A., McCord, T. B., & Hansen, G. B. 2000, *JGR*, **105**, 22541
- Hibbitts, C. A., Pappalardo, R. T., Hansen, G. B., & McCord, T. B. 2003, *JGRE*, **108**, 5036
- Hibbitts, C. A., & Szanyi, J. 2007, *Icar*, **191**, 371
- Iida, K., Yokogawa, D., Sato, H., & Sakaki, S. 2007, *CPL*, **443**, 264
- Jamieson, C. S., Mebel, A. M., & Kaiser, R. I. 2006, *ChemPhysChem*, **7**, 2508
- Jamieson, C. S., Mebel, A. M., & Kaiser, R. I. 2007a, *CPL*, **443**, 49
- Jamieson, C. S., Mebel, A. M., & Kaiser, R. I. 2007b, *CPL*, **440**, 105
- Jamieson, C. S., Mebel, A. M., & Kaiser, R. I. 2008, *CPL*, **450**, 312
- Johnson, R. E. 1990, *Energetic Charged-particle Interactions with Atmospheres and Surfaces (Physics and Chemistry in Space Planetology, Vol. 19; Berlin: Springer)*
- Jones, B. M., Kaiser, R. I., & Strazzulla, G. 2014a, *ApJ*, **781**, 85
- Jones, B. M., Kaiser, R. I., & Strazzulla, G. 2014b, *ApJ*, **788**, 170
- Kaiser, R. I., Eich, G., Gabrysch, A., & Roessler, K. 1997, *ApJ*, **484**, 487
- Kaiser, R. I., & Roessler, K. 1997, *ApJ*, **475**, 144
- Lammer, H., Chassefière, E., Karatekin, Ö., et al. 2013, *SSRv*, **174**, 113
- Leung, K., Nielson, I. M. B., & Kurtz, I. 2007, *JPCB*, **111**, 4453
- Lundin, R., Lammer, H., & Ribas, I. 2007, *SSRv*, **129**, 245
- Madey, T. E., Johnson, R. E., & Orlando, T. M. 2002, *SurSc*, **500**, 838
- McCord, T. B., Carlson, R., Smythe, W., et al. 1997, *Sci*, **278**, 271
- McCord, T. B., Hansen, G. B., Clark, R. N., et al. 1998, *JGR*, **103**, 8603
- Molina-Cuberos, G. J., Stumptner, W., Lammer, H., Kömle, N. I., & O'Brien, K. 2001, *Icar*, **154**, 216
- Montgomery, C. J., Tang, Q., Sarofim, A. F., et al. 2008, *Improved Kinetic Models for High-speed Combustion Simulation (Phase II STTR, AFRL-RZ-WP-TR-2008-2197 (Salt Lake City, UT: Reaction Engineering International))*
- Moore, M. H., & Khanna, R. K. 1991, *AcSpA*, **47**, 255
- Oba, Y., Watanabe, N., Kouchi, A., Hama, T., & Pirronello, V. 2010, *ApJ*, **722**, 1598
- Ootsubo, T., Kawakita, H., Hamada, S., et al. 2012, *ApJ*, **752**, 15
- Peeters, Z., Hudson, R. L., Moore, M. H., & Lewis, A. 2010, *Icar*, **210**, 480
- Pilling, S., Seperuelo Duarte, E., Domaracka, A., et al. 2010, *A&A*, **523**, A77
- Pinilla-Alonso, N., Roush, T. L., Marzo, G. A., Cruikshank, D. P., & Dalle Ore, C. M. 2011, *Icar*, **215**, 75
- Quirico, E., Douté, S., Schmitt, B., et al. 1999, *Icar*, **139**, 159
- Raut, U., & Baragiola, R. A. 2013, *ApJ*, **772**, 53
- Reach, W. T., Kelley, M. S., & Vaubaillon, J. 2013, *Icar*, **226**, 777
- Reddy, S. K., & Balasubramanian, S. 2014, *ChCom*, **50**, 503
- Rodríguez-García, V., Hirata, S., Yagi, K., et al. 2007, *JChPh*, **126**, 124303
- Sandford, S. A., & Allamandola, L. J. 1990, *ApJ*, **355**, 357
- Satorre, M. Á., Domingo, M., Millán, C., et al. 2008, *P&SS*, **56**, 1748
- Scipioni, F., Tosi, F., Stephan, K., et al. (the VIMS Team) 2013, *Icar*, **226**, 1331
- Selsis, F., Kaltenecker, L., & Paillet, J. 2008, *PhST*, **130**, 014032
- Seperuelo Duarte, E., Boduch, P., Rothard, H., et al. 2009, *A&A*, **502**, 599
- Sivaraman, B., Sekhar, B. N. R., Fulvio, D., et al. 2013, *JChPh*, **139**, 074706
- Smythe, E. D., Carlson, R. W., Ocampo, A., Matson, D. L., & McCord, T. B. 1998, *BAAS*, **30**, 1448
- Song, X., Li, J., Hou, H., & Wang, B. 2006, *JChPh*, **125**, 094301
- Starukhina, L. V. 2006, *AdSpR*, **37**, 50
- Strazzulla, G., & Johnson, R. E. 1991, in *Comets in the Post-Halley Era*, ed. R. L. Newburn, Jr., M. Nuegebauer, & J. Rahe (Dordrecht: Kluwer), 243
- Strazzulla, G., Leto, G., Spinola, F., & Gomis, O. 2005, *AsBio*, **5**, 612
- Swain, M. R., Deroo, P., Griffith, C. A., et al. 2010, *Natur*, **463**, 637
- Teolis, B. D., Jones, G. H., Miles, P.F., et al. 2010, *Sci*, **330**, 1813
- Wight, C. A., & Boldyrev, A. I. 1995, *JPhCh*, **99**, 12125
- Wu, C. Y. R., Judge, D. L., Cheng, B.-M., et al. 2003, *JGRE*, **108**, 5032
- Wu, J.-J., Wu, C. Y. R., & Liang, M.-C. 2011, *Icar*, **214**, 228
- Zheng, W., & Kaiser, R. I. 2007, *CPL*, **450**, 55
- Ziegler, J. F., Ziegler, M. D., & Biersack, J. P. 2010, *NIMPB*, **268**, 1818